Supplemental material for "Bound electron nonlinearity beyond the ionization threshold"

1. Experimental setup

The laser used in the experiments is a λ=800 nm Ti:Sapphire amplifier producing 42 fs, 10 mJ pulses at a 1 kHz repetition rate. A beam splitter deflects up to 90% of the energy out of the amplifier before it is compressed. This beam is compressed by an external compressor just before entering the vacuum chamber. For pump pulses, up to ~0.5 mJ is focused by a 75 cm focal length lens to a full width at half maximum (FWHM) spot size of 65 μm in the gas tube target. The other 10% of the amplifier output is compressed by the internal compressor and focused into a Xe gas cell, generating supercontinuum pulses of energy ~1 μJ covering the range 500-700 nm. This is split into probe and reference pulses using a Michelson interferometer and sent into the vacuum chamber, focused by a 50 cm focal length lens to a spot size of ~200 μm, which overfills the hole in the target. The pump and probe beams are linearly polarized with parallel polarization. The probe pulse spectral phase is characterized by time-dependent cross phase modulation [21]. The spectral phase is well fit by $\varphi(\omega) = \beta_2(\omega - \omega_0)^2 + \beta_3(\omega - \omega_0)^3$, where β_2 = 1050 fs^2, β_3 = 100 fs^3, ω_0 = 3.15 fs^{-1}.

The gas flow target is made from a cylindrical stainless steel tube with 89 μm thick walls, pinched to the desired outer thickness of 200-400 μm and then drilled by the laser, producing 80-200 μm diameter holes in the front and back walls. Gas is slowly fed from one end of the tube and the other end is terminated. The target assembly is mounted on a translation stage in a vacuum chamber, with a flexible tube connecting it to a source of gas. The chamber is pumped by a roots blower. To avoid long-lived, cumulative thermal effects that can alter the gas density [25], the repetition rate of the pump laser is reduced to 20 Hz.

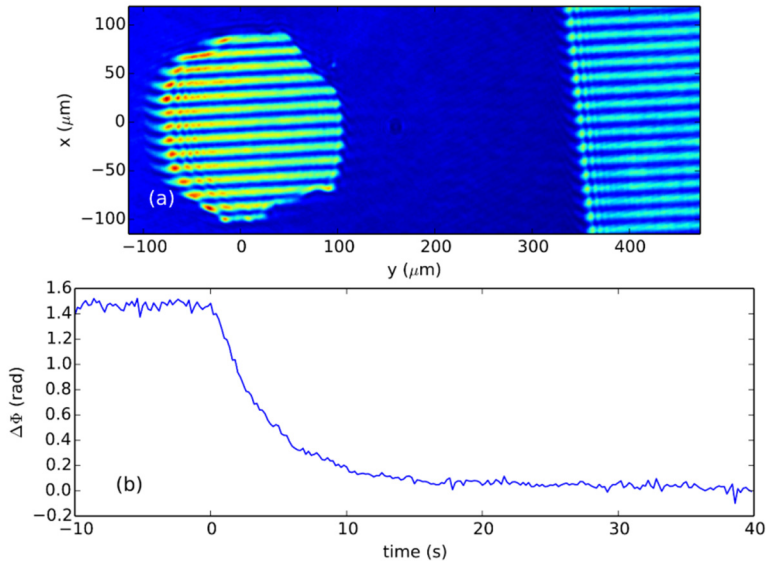

Figure S1. (a) Typical interferogram showing light propagating through the hole (left) and around the target (right). (b) Phase shift through the target measured in N_2 as a function of time as the gas input is shut off suddenly at t = 0 s.

The gas density distribution in the gas tube hole and outside the tube is characterized by folded wavefront interferometry, using a 635 nm diode laser. The measured phase shift is proportional to the axially integrated gas density sampled by the 635 nm probe laser as it propagates through the gas.

To determine the integrated gas density through the target, the probe beam propagates through the hole (along the path of the SSSI probe light) with part of the beam outside the tube. The interference between these two beam segments provides the phase shift and refractive index change from which the mean target density N_0 is determined [8]. Typical longitudinal interferometry results are shown in Fig. S1.

Figure S2 shows the phase shift imposed on the probe beam directed perpendicular to the hole axis and skimming one side of the tube, showing that the gas density drops to ~$0.5N_0$ near the plane of the hole and falls roughly exponentially, reaching $0.2N_0$ about 100 μm beyond the hole.

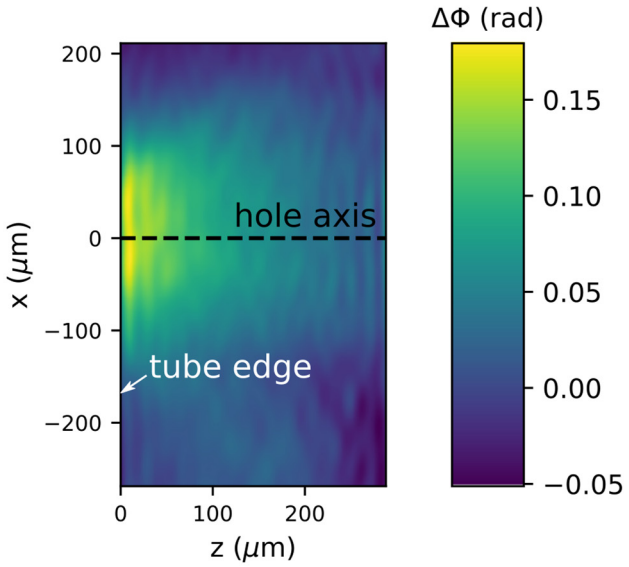

Figure S2. Phase shift image of density profile of gas flowing out of the tube hole, showing that the N_2 density falls off quickly outside the tube (the tube edge is at $z = 0$, and the hole center is at $x = 0$). The vertical ripples are from diffraction from the tube edge.

The flow gas pressure (density) in the target is adjusted to maximize the probe phase shift while limiting ionization-induced refraction of the pump and probe. Typically this demanded running at lower gas pressure at high laser intensities and at higher pressure for lower laser intensities. A roots pump maintains a background chamber pressure of <1 mbar (~100 Pa). The effective interaction length L_{eff} is much smaller than the pump and probe confocal parameters of 30 mm and 200 mm respectively, helping ensure that the pump intensity is independent of the axial coordinate within the gas, improving the time resolution [S1].

To record and monitor the pump beam shape during the experiment, we image residual pump (~0.1%) light transmitted through the dichroic mirror DM1 in Fig. 1 of the main text using a CCD camera (not shown in the figure) placed at the equivalent focal plane of the pump focusing lens. We refer to this as the pre-target camera. Approximately 0.1% of the 800 nm pump beam is transmitted through dichroic mirror that separates the pump and probe light (DM2 in Fig. 1 of the main text). This residual pump light is reflected by another dichroic mirror (DM3) and imaged using another CCD camera (the post-target camera) placed at the equivalent plane of the entrance slit of the imaging spectrometer. We find that for

the peak intensities and gases used in the experiment, the images of the pump beam pre- and post-target agree within error. At higher laser pulse energy, effects from plasma defocusing are observed.

For each 2D+1 data set, a total of ~10^4 shots is used to construct $\Delta\Phi(x,y,t)$, as discussed in the main text. For each laser shot, an image of the pump spot is also captured, enabling measurement of y_i as the probe beam is swept back and forth, and allowing post-collection compensation in the data analysis of pump beam intensity and pointing fluctuations and drift. The interferograms are sorted into ~30 bins by their y_i value, as determined from the corresponding pump spot image for each laser shot. The interferograms in each bin are summed before phase extraction. The number of interferograms in each y_i bin varies from tens to hundreds.

Recording the full 2D+1 phase shift and amplitude change of the probe beam has multiple advantages. Among them are that the spatial peak of the pump spot is easily located, even in the presence of pointing drift, and that a single 2D phase shift profile contains many intensity points.

2. Experimental results for Kr, Xe, N_2, and O_2

Experimental results, in the same format as the Ar results shown in Fig. 2 of the paper, are shown in Figs. S3-S6 for the other gases studied. The bound electronic response is relatively larger in Kr and Xe than in Ar, but otherwise the results are qualitatively similar. The molecular gases N_2 and O_2 have an additional delayed rotational response that peaks ~80 fs after the peak of the pump pulse [8, 23]. Movies showing the evolution of $\Delta\Phi(x,y,t)$ for each of these data sets are provided in the supplementary materials.[1]

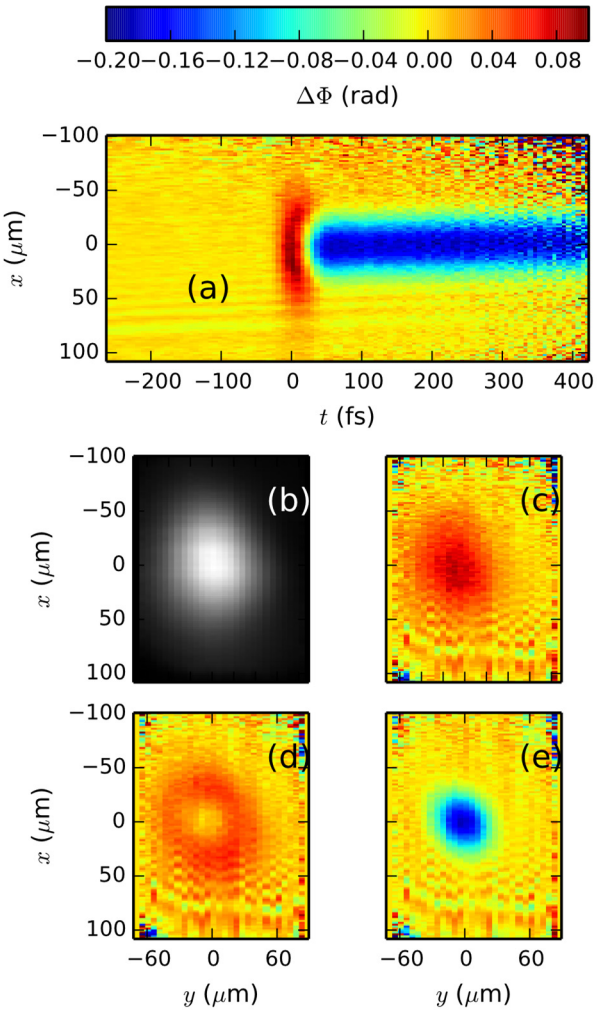

Figure S3. Results for Kr at a pump peak intensity of 84 TW/cm^2. (a) Measured spatiotemporal phase shift $\Delta\Phi(x,y_0=0,t)$. (b) Image of the pump spot at the gas target, showing that the Kerr response follows the pump intensity profile. (c) Phase shift $\Delta\Phi(x,y,t_0 - 14$ fs), showing the Kerr response dominating. (d) Phase shift $\Delta\Phi(x,y,t_0+21$ fs), showing the Kerr response on the wings and the growing plasma phase shift in the center of the beam. (e) Phase shift $\Delta\Phi(x,y,t_0+100$ fs), showing the negative plasma phase shift long after the pump pulse.

[1] These can be found at http://lasermatter.umd.edu/publications.html#bound_electron_supplementary , or at the APS-PRL website.

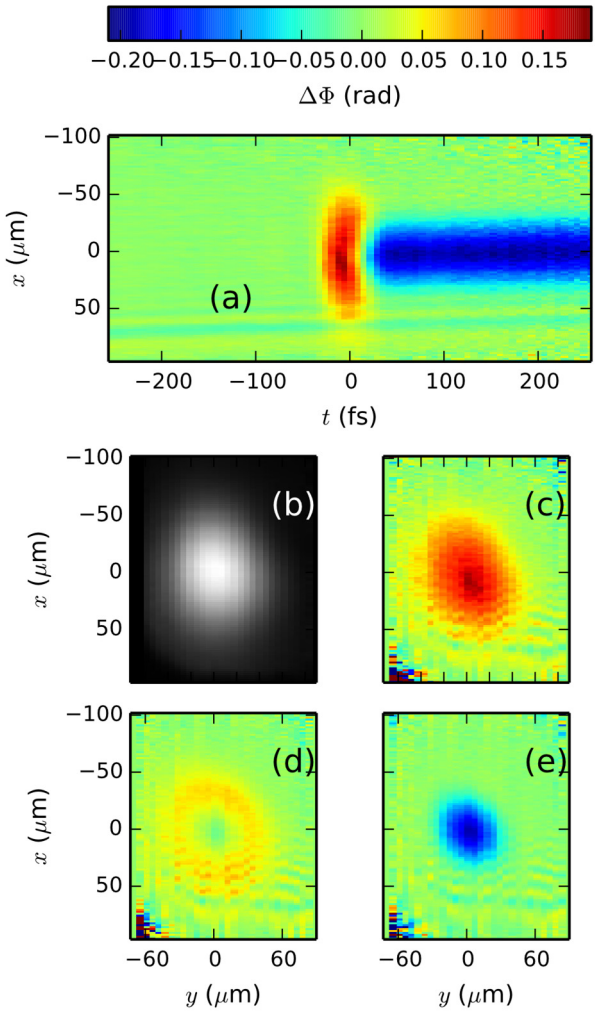

Figure S4. Results for Xe at a pump peak intensity of 50 TW/cm^2. (a) Measured spatiotemporal phase shift $\Delta\Phi(x,y_0=0,t)$. (b) Image of the pump spot at the gas target, showing that the Kerr response follows the pump intensity profile. (c) Phase shift $\Delta\Phi(x,y,t_0 - 14$ fs), showing the Kerr response dominating. (d) Phase shift $\Delta\Phi(x,y,t_0+14$ fs), showing the Kerr response on the wings and the growing plasma phase shift in the center of the beam. (e) Phase shift $\Delta\Phi(x,y,t_0+100$ fs), showing the negative plasma phase shift long after the pump pulse.

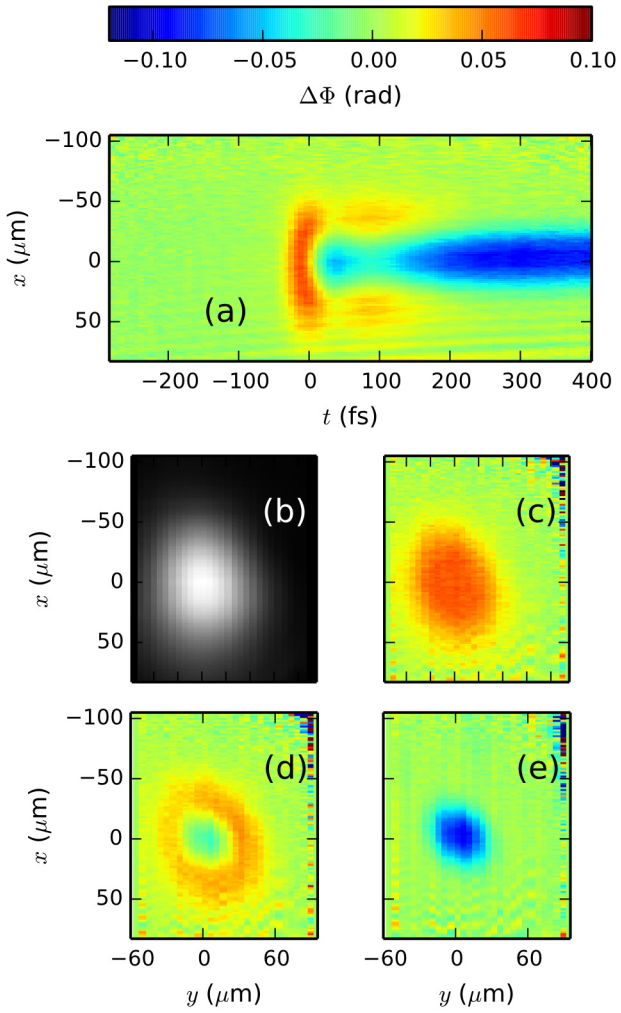

Figure S5. Results for N_2 at a pump peak intensity of 114 TW/cm^2. (a) Measured spatiotemporal phase shift $\Delta\Phi(x,y_0=0,t)$. (b) Image of the pump spot at the gas target, showing that the Kerr response follows the pump intensity profile. (c) Phase shift $\Delta\Phi(x,y,t_0 - 14$ fs), showing the Kerr response dominating. (d) Phase shift $\Delta\Phi(x,y,t_0+14$ fs), showing the Kerr response on the wings and the growing plasma phase shift in the center of the beam. (e) Phase shift $\Delta\Phi(x,y,t_0+280$ fs), showing the negative plasma phase shift long after the pump pulse and the bound electronic and rotational response.

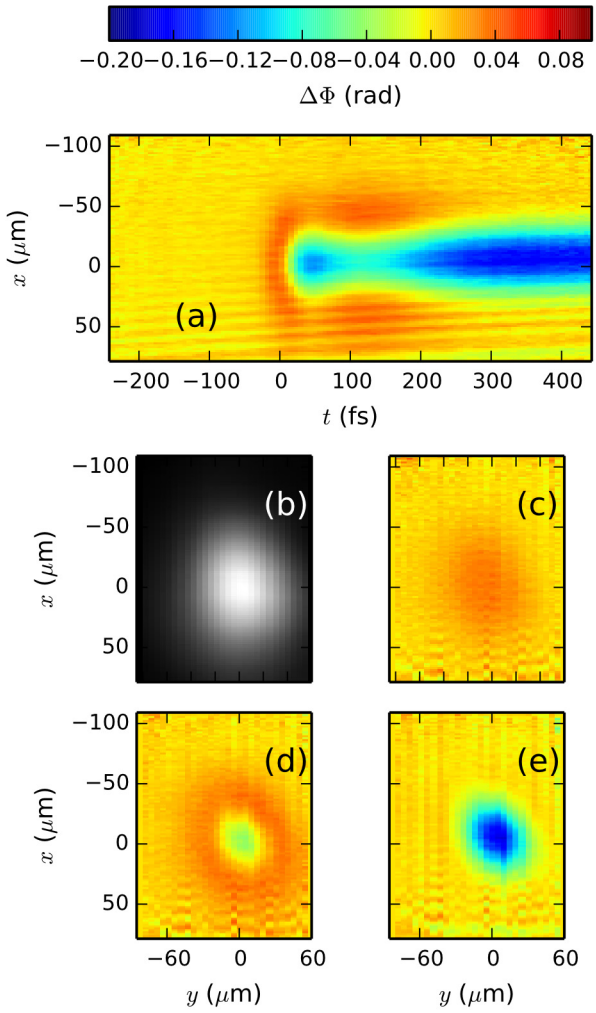

Figure S6. Results for O_2 at a pump peak intensity of 88 TW/cm^2. (a) Measured spatiotemporal phase shift $\Delta\Phi(x,y_0=0,t)$. (b) Image of the pump spot at the gas target, showing that the Kerr response follows the pump intensity profile. (c) Phase shift $\Delta\Phi(x,y,t_0 - 14$ fs), showing the Kerr response dominating. (d) Phase shift $\Delta\Phi(x,y,t_0+14$ fs), showing the Kerr response on the wings and the growing plasma phase shift in the center of the beam. (e) Phase shift $\Delta\Phi(x,y,t_0+350$ fs), showing the negative plasma phase shift long after the pump pulse and the bound electronic and rotational response.

3. Fits of ionization yield data

A full intensity scan for a gas species consists of multiple 2D+1 data sets, each at a different nominal peak space-time laser intensity. A total of 9 data sets were used for Ar, 4 for Kr, 6 for Xe, 9 for N_2, and 8 for O_2 to generate Figs. 3 and 4.

The measured ionization yield Y over the intensity range measured here is very well-fit by the expression

$$Y = c_1 I_0^m \qquad \textbf{(S1)}$$

as shown by the dashed curves in Fig. 3 of the paper. Here I_0 is the temporal peak intensity that occurred at a particular x, y location, so that *each* 2D+1 SSSI trace $\Delta\Phi(x,y,t_1)$ contains many I_0, Y pairs, where $t_1 >$ 50 fs for the noble gases and $t_1 > 250$ fs for N_2 and O_2 The fit for each gas to Eq. (S1) yields parameters c_1 and m given in Table S1. The point of the expression used for Y is not to advance a multiphoton-ionization (MPI)-like model for ionization; it is to provide an analytic model fit to the ionization yield data to enable separation of the bound and free electron contributions. In fact, the best fit values for m are notably smaller than their corresponding multiphoton ionization values (m_{MPI}) for each species (also shown in Table S1), indicating the significant contribution of tunneling ionization.

Examples of the time-dependent phase shift $\Delta\Phi(x_0=0,y_0=0,t)$ in Kr, Xe, N_2, and O_2, along with fits to the bound response + ionization model described in the main text, are shown in Figs. S7, S8, S9, and S10. These are equivalent to Fig. 4ab in the main text. Panel (a) in each figure shows the response at an intensity below the ionization threshold. Figures S7a and S8a for Kr and Xe show the Kerr response, which follows the intensity pulse envelope. For N_2 and O_2 in Figs. S9a and S10a, the initial peak, which is the prompt Kerr response, is followed by the delayed rotational response. Panel (b) in each figure shows the response as the peak laser intensity is increased to produce growing levels of ionization. For the atomic gases Ar, Kr and Xe, the time-dependent refractive index shift data is fit to

$$\Delta n(t) = \Delta n_K e^{-t^2/\tau^2} + \Delta n_p (1 + \mathrm{erf}[m^{1/2} t/\tau])/2\,, \qquad \textbf{(S2)}$$

while for N_2 and O_2, it is fit to

$$\Delta n(t) = \Delta n_K e^{-t^2/\tau^2} + \Delta n_{rot} R(t) + \Delta n_p (1 + \mathrm{erf}[m^{1/2} t/\tau])/2\,, \qquad \textbf{(S3)}$$

where in Eq. S3 both Δn_K and Δn_{rot} are fitting parameters and $R(t)$ is the rotational response function [8, 23] convolved with a Gaussian with a FWHM of 42 fs. Note that the fit was optimum assuming a gas temperature of 200 K (the shape of the rotational response function is sensitive to temperature because the initial population of rotational states is affected). This indicates cooling of the gas as it expands into the vacuum chamber through the holes in the target.

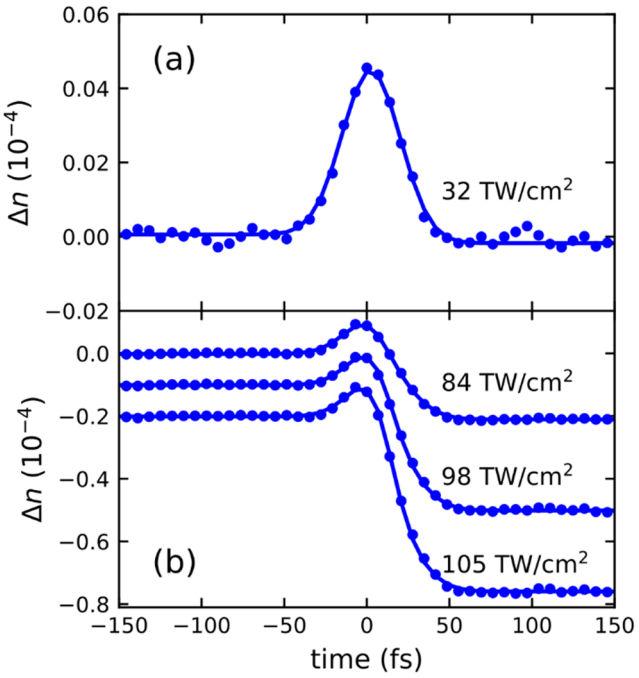

Figure S7. Kr response during pump pulse. (a) Nonlinear index shift in Kr vs. time for peak intensity 32 TW/cm^2 (dots), below the ionization threshold, and a fit to a Gaussian pulse with τ_{FWHM} =42 fs (solid line). (b) Nonlinear index shift vs. time (dots) and fits to Eq. S2 (solid lines), where Δn_k is a fitting parameter. The curves have been offset vertically for clarity.

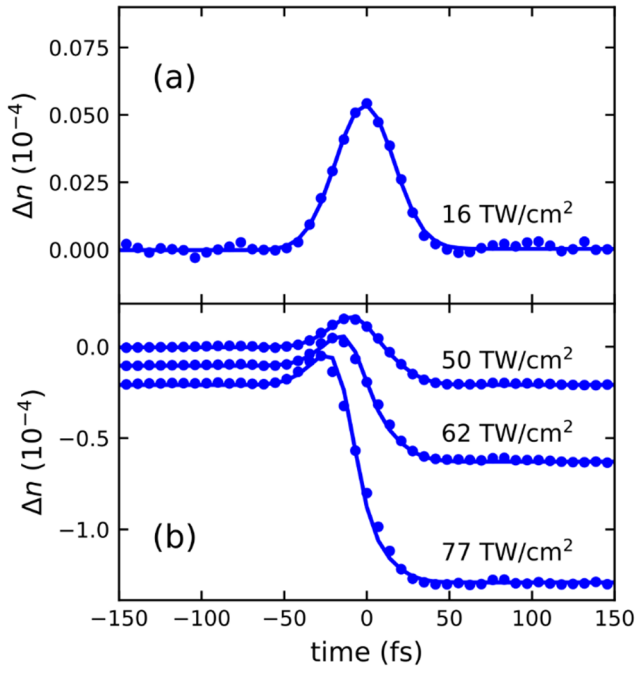

Figure S8. Xe response during pump pulse. (a) Nonlinear index shift in Xe vs. time for peak intensity 16 TW/cm^2 (dots), below the threshold for ionization, and a fit to a Gaussian pulse with τ_{FWHM} =42 fs (solid line). (b) Nonlinear index shift vs. time (dots) and fits to Eq. S2 (solid lines), where Δn_k is a fitting parameter. The curves have been offset vertically for clarity.

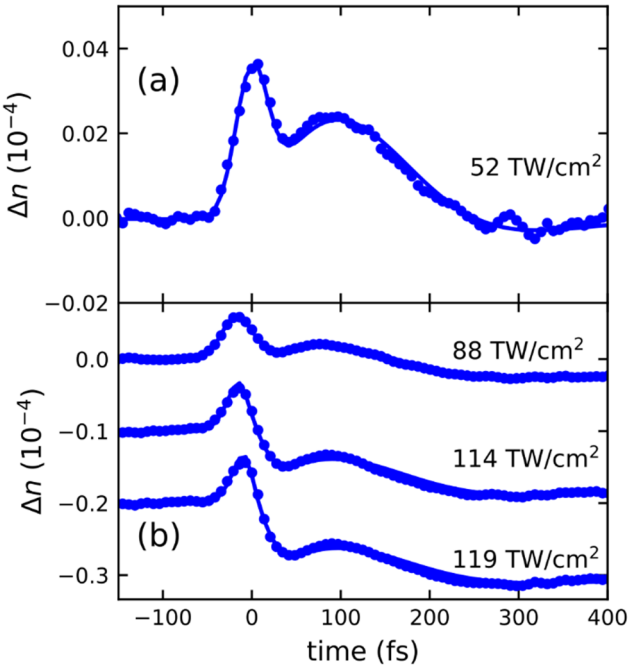

Figure S9. N_2 response during pump pulse. (a) Nonlinear index shift in N_2 vs. time for peak intensity 52 TW/cm^2 (dots), below the threshold for ionization, and a fit to Eq. S3 for Δn_p=0 and a Gaussian pulse with τ_{FWHM} =42 fs. (b) Nonlinear index shift vs. time (dots) and fits to Eq. S2 (solid lines), where Δn_k and Δn_{rot} are fitting parameters. The curves have been offset vertically for clarity.

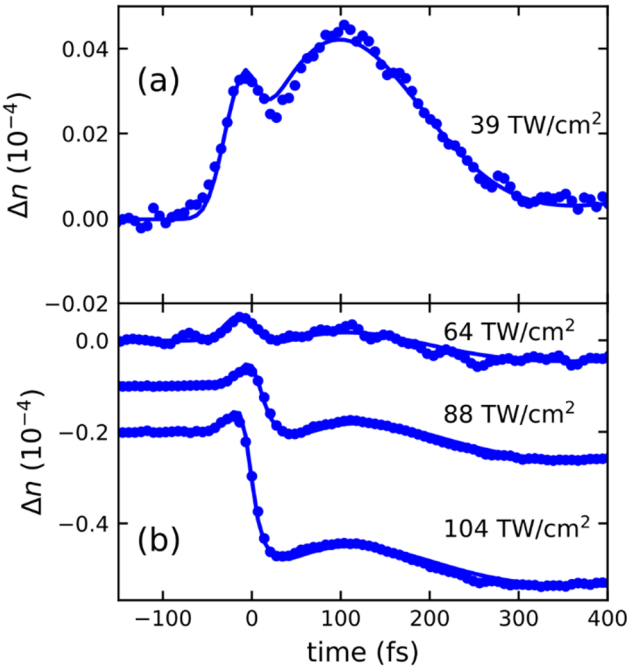

Figure S10. Response during pump pulse. (a) The nonlinear index shift in O_2 as a function of time for peak intensity of 39 TW/cm^2, below the threshold for ionization, and a fit to a Gaussian with FWHM 42 fs. (b) Nonlinear index shift vs. time (dots) and fits to Eq. S2 (solid lines), where Δn_k and Δn_{rot} are fitting parameters. The curves have been offset vertically for clarity.

Also shown in Table S1 are values of n_2 extracted from fits of the bound response to a linear intensity dependence for datasets spanning the full intensity range from no ionization to significant ionization; the fits are to the bound index shift versus intensity data points shown in Fig. 4cd in the main text. Notably, these effective values of n_2 for Ar, Kr, and Xe are higher than the values measured for intensities below the onset of ionization [9], owing to an apparent greater than linear intensity dependence of the bound electron response above the ionization threshold, the detailed scaling of which requires more precise measurements. However, for the molecules, the effective n_2 value for N_2 over the full intensity range is the same as at sub-ionization intensities, whereas the full range value in O_2 is lower than at sub-ionization intensities [8].

Table 1. Summary of results

Gas	c_I [(cm^2/TW)$^{-m}$]	m_{fit}	m_{MPI}	n_2 (cm^2/W) (full intensity range from below to above ionization threshold)	n_2 (cm^2/W) [8,9] (Below ionization threshold)
Ar	2.05×10^{-13}	5.14	11	$(12.2\pm1.6)\times10^{-20}$	$(9.7\pm1.2)\times10^{-20}$
Kr	5.17×10^{-11}	4.43	9	$(2.7\pm0.4)\times10^{-19}$	$(2.2\pm0.4)\times10^{-19}$
Xe	5.47×10^{-10}	4.36	7	$(7.1\pm0.9)\times10^{-19}$	$(5.8\pm1.1)\times10^{-19}$
N_2	5.7×10^{-16}	6.28	11	$(7.4\pm1.0)\times10^{-20}$	$(7.4\pm0.9)\times10^{-20}$
O_2	9.6×10^{-11}	4.09	7	$(5.8\pm0.8)\times10^{-20}$	$(9.5\pm1.2)\times10^{-20}$

Supplemental references

[S1] K. Kim, I. Alexeev, and H. M. Milchberg, "Single-shot measurement of laser-induced double step ionization of helium," Opt. Express **10**, 1563 (2002).